

Self-supervised Tumor Segmentation through Layer Decomposition

Xiaoman Zhang, Weidi Xie, Chaoqin Huang, Ya Zhang, and Yanfeng Wang

Abstract—In this paper, we propose a self-supervised approach for tumor segmentation. Specifically, we advocate a zero-shot setting, where models from self-supervised learning should be directly applicable for the downstream task, *without* using any manual annotations whatsoever. We make the following contributions. *First*, with careful examination on existing self-supervised learning approaches, we reveal the surprising result that, given suitable data augmentation, models trained from scratch in fact achieve comparable performance to those pre-trained with self-supervised learning. *Second*, inspired by the fact that tumors tend to be characterized *independently* to the contexts, we propose a scalable pipeline for generating synthetic tumor data, and train a self-supervised model that minimises the generalisation gap with the downstream task. *Third*, we conduct extensive ablation studies on different downstream datasets, BraTS2018 for brain tumor segmentation and LiTS2017 for liver tumor segmentation. While evaluating the model transferability for tumor segmentation under a low-annotation regime, including an extreme case of zero-shot segmentation, the proposed approach demonstrates state-of-the-art performance, substantially outperforming all existing self-supervised approaches, and opening up the usage of self-supervised learning in practical scenarios.

Index Terms—Self-supervised learning, 3D tumor segmentation

I. INTRODUCTION

In medical image analysis, segmentation has been treated as one of the most important intermediate representations for obtaining reliable clinical measurements, for example, size, shape, location, texture characteristics, or even growth rate of certain structures or anatomy, *etc.* Such measurements can assist clinicians to make assessments of corresponding diseases and better treatment plans.

In this paper, we consider the problem of *segmenting tumors* in 3D volumes. In the recent literature, remarkable progress has been made with the use of deep neural networks [1]–[4], however, these successful approaches often fall into the paradigm of supervised learning, which requires a large number of manually annotated volumes for training. On tumor segmentation, acquiring annotations can often be a prohibitively expensive process, due to the large variability

X. Zhang, C. Huang, Y. Zhang, Y. Wang are with the Cooperative Medianet Innovation Center, Shanghai Jiao Tong University and Shanghai AI Laboratory, Shanghai 200240, China. (Email: {xm99sjtu, huangchaoqin, ya_zhang, wangyanfeng}@sjtu.edu.cn).

W. Xie is with Visual Geometry Group, Department of Engineering Science, University of Oxford, UK. (Email: weidi@robots.ox.ac.uk).

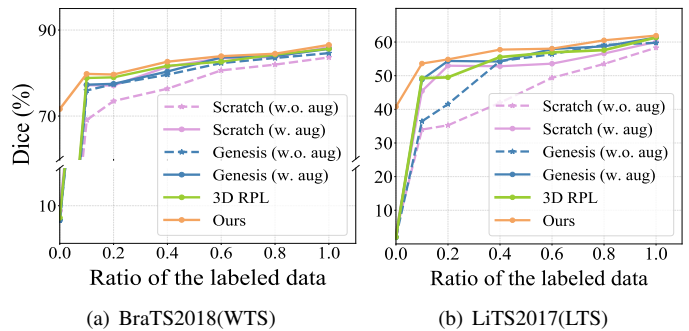


Fig. 1. Segmentation results of tumor segmentation on BraTS2018 and LiTS2017 datasets when fine-tuning on an increasing number of annotated data. Pretraining with SSL methods does not always improve the performance in all the supervision levels. Please refer to the detailed numbers in Table III.

in tumors' shape, size and location [5], posing limitations on the scalability of such training paradigm.

To alleviate the dependency on manual annotations in supervised training, the research community has recently shifted to a new learning paradigm, namely, self-supervised learning (SSL), with the goal of learning effective visual representation purely from raw data [6]–[11], by solving some artificially defined proxy tasks. Generally speaking, the existing self-supervised approaches [12]–[14] in medical image analysis have predominantly followed a two-stage training paradigm, where the model is firstly pre-trained on unlabelled data by solving certain proxy task, and further adapted to the downstream segmentation task through *fully supervised fine-tuning*, that is to say, a large number of manual annotations remain prerequisite.

We carefully examine various state-of-the-art methods, with the number of labeled data controlled in the fine-tuning stage, for example, evaluate the performance by fine-tuning on 0%, 10%, 20%, ..., 100% annotations. As shown in Fig. 1, self-supervised pre-training (*e.g.* 3D Relative Location Prediction [9], Genesis [10]) indeed demonstrates superior generalisation over the scratch model that is trained with simple data augmentations, however, such advantage quickly diminishes as we introduce more data augmentations into the from-scratch training procedure. While it may seem surprising at a first glance, we argue this is in fact a fair comparison between two-stage training and from-scratch training, as heavy data augmentations are usually essential in self-supervised pre-training. Based on such phenomenon, several questions naturally arise: *given the downstream task is tumor segmentation, what proxy task is more appropriate for self-supervised training, and when*

is such self-supervised training useful?

We address these questions from two aspects:

First, to fully deliver the merits of self-supervised learning, one should define the proxy task in a way that minimises the generalisation gap with the considered downstream task. Inspired by the observation that tumors are often characterised independently to their contexts, we propose a scalable pipeline for generating synthetic training samples, by blending artificial “tumors” into normal organ, resembling the classical idea of layer representation [15]. During self-supervised learning, we train a generative model to invert such generation process, *i.e.* separately reconstructing the tumor and organ, and predicting the tumor mask used for linear compositing. Note that, once warmed up with synthetic data, the training can also be applied on the real tumor volume, with the proxy task turning to a “layer-based” reconstruction, *i.e.* to minimise the discrepancy between the reconstruction and the input tumor sample. During inference, such self-supervised model enables to infer the tumor mask on real-world samples, *without* any fine-tuning whatsoever, namely, zero-shot tumor segmentation. We term this ability as the model’s *generalisability*.

Second, we observe that self-supervised learning really shines under a low-annotation regime. As shown in Fig I, when only 10% of annotations are available for fine-tuning, all existing self-supervised approaches demonstrate more efficient use of the available data, demonstrating superior *transferability*.

To summarise, in this paper, we make the following contribution: *First*, we carefully examine several existing self-supervised learning approaches and reveal the surprising result: models trained from scratch in fact achieve comparable performance to those pre-trained with self-supervised learning, given suitable data augmentation is adopted; *Second*, we take inspiration from “layer-decomposition”, and propose a scalable pipeline for generating synthetic tumor data, which enables to train our self-supervised model with minimal generalisation gap with the downstream task, supporting zero-shot tumor segmentation; *Third*, we evaluate our proposed approach on two downstream datasets, BraTS2018 [16] for brain tumor segmentation and LiTS2017 [17] for liver tumor segmentation, showing superior performance over all existing self-supervised approaches on *transferability* and *generalisability*. *Fourth*, we have conducted comprehensive ablation studies on the critical components for data simulation, and the effects of the proposed loss functions. We would refer readers to the project page for qualitative results, and codes for reproducing our results: <https://xiaoman-zhang.github.io/Layer-Decomposition/>.

II. RELATED WORK

A. Supervised 3D Tumor Segmentation

Automatic tumor segmentation in medical imaging is a very challenging task due to the fuzzy boundary and high variation in size, shape and location. In the recent literature, the progress has been mainly driven by the success of deep neural networks [18]–[20], for example, Isensee *et al.* [20] proposed nnU-Net, which can dynamically adapt itself to any given segmentation task. Li *et al.* [18] introduced a

hybrid densely connected UNet (H-DenseUNet) that enables to probe the hierarchical intra-slice features for liver and tumor segmentation. However, training such deep networks often requires a large number of data with annotations available, which is expensive and time-consuming to acquire, significantly limiting the scalability of supervised learning.

B. Semi-supervised 3D Tumor Segmentation

Several efforts have attempted to address these challenges in semi-supervised setting [21]. Specifically, in semi-supervised segmentation, only a smaller set of training samples are provided manual annotations, and the goal is to improve the model’s performance with large amounts of unlabeled data. Min *et al.* [22] adopted the idea of self-training, specifically, reliable pseudo labels are firstly generated for unlabelled data by hierarchical distillation, and then mixed data is used to retrain the proposed two-stream mutual attention network. Chen *et al.* [23] proposed to use unlabelled data by simultaneously optimising supervised segmentation and unsupervised reconstruction tasks. These methods, however, still require a handful of annotations.

C. Self-supervised Representation learning

Self-supervised learning [7]–[11], [24]–[27] aims to learn effective visual representation from raw data *without* using manual annotations. In general, existing frameworks in medical imaging follow a two-stage training procedure, first, a model is trained by solving some predefined proxy task on a large-scale dataset, the learned representation is further fine-tuned for the downstream tasks with annotated data. Specifically, [8], [10] proposed to restore the original image from artificial jitterings, *e.g.* rotation, patch shuffling and deformation. Bai *et al.* [24] used anatomical position prediction as a pretext task for cardiac MR image segmentation. Taleb *et al.* [9] developed 3D versions algorithms for five different self-supervised methods, including 3D Contrastive Predictive Coding, 3D Rotation prediction, 3D Jigsaw puzzles, Relative 3D patch location, and 3D Exemplar networks. Note that, in these aforementioned approaches, proxy tasks are defined with limited prior knowledge from downstream task, thus, manual annotations are still required for fine-tuning. In contrast to these two-stage training, we target direct generalisation, by that we mean, once trained to solve the proxy tasks, the self-supervised model should be able to segment tumors *without* fine-tuning on any annotated data, *i.e.* zero-shot tumor segmentation. In addition, when a small number of annotated data is available, our proposed model can be fine-tuned to further boost the segmentation performance.

D. Anomaly Detection

In the literature, anomaly detection [28]–[31] has been treated as an alternative to unsupervised tumor segmentation, with the underlying assumption that, images from healthy patients tend to have a similar pattern. In general, there are two lines of research, namely, generative or discriminative training. Specifically, In generative training, autoencoders [32], [33] are

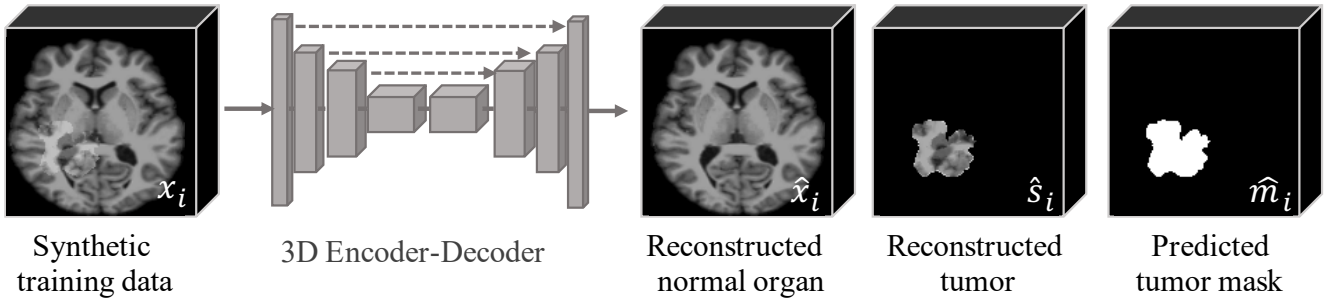


Fig. 2. Illustration of the general idea. Our model takes the synthetic training data x_i as input, and outputs the reconstruction of normal organ \hat{x}_i , tumor \hat{s}_i and the prediction of tumor mask \hat{m}_i . During inference, our pre-trained model can directly generalise to real tumor data, *i.e.* the prediction of tumor mask is treated as the segmentation result.

trained to reconstruct the normal samples, with anomalies being the regions with high reconstruction error. In [29], implicit representation is adopted to learn relevant anatomical features for 3D unsupervised anomaly detection. As an alternative, discriminative models are trained on generated abnormal images, using pseudo labels introduced during the data synthesis process as supervision [34]–[36]. In [34], training data are synthesised by mixing super-pixels from the original image, and the model is trained to detect and localise the simulated lesions. Tan *et al.* [35] proposed to train a segmentation model that directly infers the mask for anomaly region. Specifically, the authors paste random patches into the normal image with Poisson blending, and task the network to detect such subtle irregularities. In contrast, our proposed approach takes the benefit of both worlds, we can not only learn the representation of the normal image through the reconstruction channel, but also predict the segmentation mask of the detected anomalies, and demonstrate superior performance compared to the above approaches.

III. METHODS

In this paper, we propose a self-supervised approach to learn effective representation for tumor segmentation. Our key observation is that tumors are usually characterised by a region with different intensities or textures to the nearby tissue, *i.e.* independent to the surrounding contexts, as a consequence, we treat each tumor sample as a composition of tumor and normal organ, and train a model to decompose the sample into tumor, health organ, along with mask for linear blending.

Formally, given a set of 3D volume samples, $\mathcal{D} = \{x_1, x_2, \dots, x_N\}$, where $x_i \in \mathbb{R}^{H \times W \times D \times 1}$, the goal is to decompose the input to three elements, such that, their linear combinations can reconstruct the input sample (Eq. (2)):

$$\hat{x}_i, \hat{s}_i, \hat{m}_i = \Phi(x_i) \quad (1)$$

$$\hat{m}_i \cdot \hat{x}_i + (\mathbb{1} - \hat{m}_i) \cdot \hat{s}_i = x_i \quad (2)$$

where $\Phi(\cdot)$ is the parameterised model, x_i refers to the input tumor sample, \hat{x}_i is the reconstruction of normal organ, \hat{s}_i is the reconstructed tumor, as a side product, \hat{m}_i ends up to be the mask for tumor segmentation. In practise, given the strong representation capability of deep neural networks, naïvely training $\Phi(\cdot)$ with real tumor data may lead to trivial solutions, for example, $\hat{x}_i = x_i$, $\hat{m}_i = \mathbb{1}$, as we have neither

the corresponding image of organ, nor the tumor mask. We thus consider to use synthetic data, where artificial blend the “tumors” into the normal organ with full control, *i.e.* ground truth tumor, organ image and mask are available for training, as illustrated in Fig. 2.

In the following sections, we will start by introducing the data simulation process in Section III-A, then present the details of self-supervised learning in Section III-B.

A. Data Simulation

In medical imaging, tumors vary in size from a tiny nodule to a large mass with different shapes, and often appear distinct from the surrounding normal tissues. This motivates the idea of simulating tumor images by blending artificial anomalies into the normal organ, as illustrated in Fig. 3 (a). In order to artificially imitate a tumor sample, we randomly crop a region from one image and paste it to another one. In the following paragraphs, we will elaborate the two essential elements for such data simulation, namely, generate proper tumor shape, and paste realistic texture onto it.

Shape Simulation. To simulate the shape of tumors, we construct 3D masks of random size and position with non-smooth boundaries, as shown in Fig. 3 (b). We first pick a random point in the region-of-interest, *i.e.* on the target organ, as the center coordinate of the mask. Then, we produce a geodesic polyhedron by subdividing the edges of an icosahedron and projecting each vertex onto a parametric sphere of unit radius centered on the selected point. We refer the readers to [36] for more details. The polyhedron is further perturbed with simplex noise to create a non-smooth surface that more closely resembles the appearance of the real tumor. In addition, we apply transformations like random rotation and scaling to further modify its orientation and volume. Finally, the generated polyhedron is converted to a 3D binary mask (m_i) that indicates the tumor’s shape and position. Next, we will describe the detail to texture it.

Texture Simulation. To simulate the texture of tumors, we assume that a set of images of normal organ are accessible, *e.g.* $\mathcal{D}_{\text{normal}} = \{x_{n_1}, x_{n_2}, \dots\}$. In the following, we describe the tumor texture simulation process for a sampled normal image x_{n_i} , with the simulated tumor mask m_i from previous shape simulation. Specifically, we construct the texture by

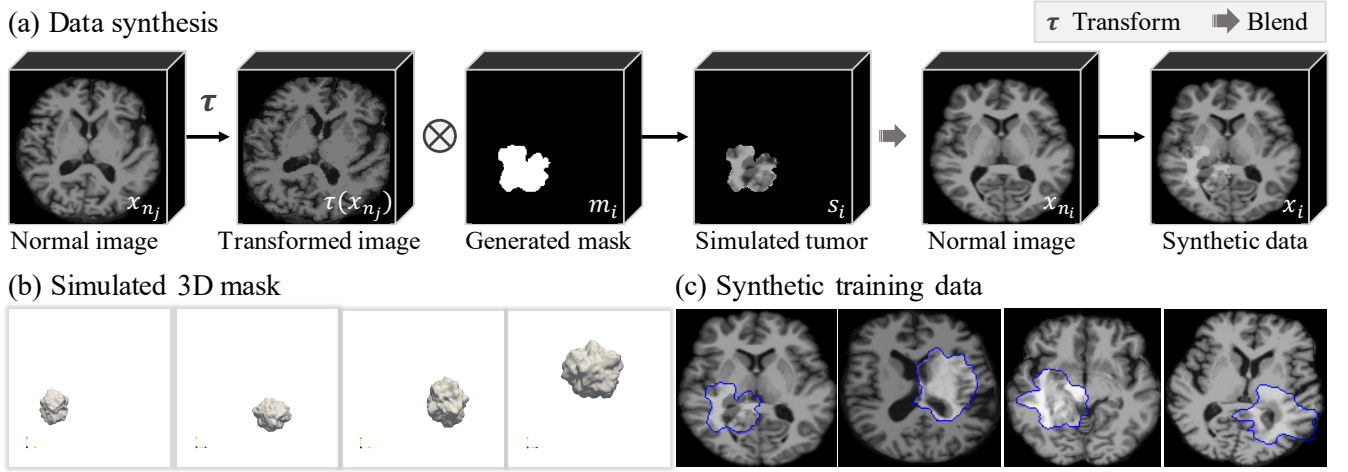


Fig. 3. (a) Data synthesis pipeline. We first simulate the tumor with a transformed image and a generated mask, which provide texture and shape respectively. Then the data is composed by blending the simulated tumor into the normal image. (b) Visualization of the simulated 3D masks with various shapes, sizes and locations. (c) Visualization of synthetic images. Blue contour denotes the mask of the simulated tumor.

borrowing from another randomly selected normal image x_{n_j} (to ensure the independence with the normal region) as:

$$s_i = m_i \cdot \tau(x_{n_j}) \quad (3)$$

where $\tau(\cdot)$ denotes a transformation function, and s_i ends up to be the synthetic tumor with texture.

We adopt three commonly-used transformations as $\tau(\cdot)$, namely, linear transformation, elastic deformation and Gaussian blur, together controlling the difficulty level for the self-supervised proxy task. Linear transformation maps the intensity of the selected normal image x_{n_j} to the desired range, which can be formulated as:

$$\tau_{LT}(x_{n_j}) = \frac{r \cdot \text{Mean}(x_{n_i})}{\text{Mean}(x_{n_j})} \cdot x_{n_j} \quad (4)$$

where $r \in (a, b)$ is the normalise ratio, $\text{Mean}(\cdot)$ denotes the average intensity. This simple transformation is the key to simulate anomalies, for example, if the tumor intensity is very different from the normal organ, the task can be trivially solved, while if the intensity is very close to the organ, the model would struggle to separate them, as it violates the assumption that tumor and organ are often *independent*. The Gaussian blur aims to remove the high-frequency signals, such as sharp boundary, strong textures, and Elastic deformation further augments the shape of tumors.

Composition. With the generated tumor s_i , we can thus generate the training sample x_i by blending the tumor into normal image x_{n_i} with an alpha mask, *i.e.* processing the generated binary tumor mask with a variable mixing parameter $\alpha \in [0, 1]$.

$$x_i = (1 - \alpha \cdot m_i) \cdot x_{n_i} + \alpha \cdot m_i \cdot s_i \quad (5)$$

Note that, to avoid abusing the notations, we here use the same ones as in Eq. (1) and Eq. (2), however, here x_i, s_i and m_i come from simulation with ground truth being available, it is trivial to train the decomposition model ($\Phi(\cdot)$) with supervision on all the output elements. Amazingly, we show

that, simply training on these synthetic data already enables the model to directly generalise towards real data, with the inferred map as tumor segmentation mask. In the next section, we will detail the training procedure.

B. Learning to Decompose

Given the synthetic dataset described in the previous section, *e.g.* $\mathcal{D}_{\text{synthetic}} = \{d_1, d_2, \dots, d_n\}$, where $d_i = \{x_i, x_{n_i}, s_i, m_i\}$, refers to the set consisting synthetic tumor sample, normal organ image, simulated tumor and mask respectively. We propose to train a network $\Phi(\cdot)$ that separately reconstructs the normal organ and tumor, and outputs the tumor mask. The proxy task is considered to invert the data simulation process, as illustrated in Eq. (1) and Fig. 2 (b).

In detail, we adopt standard L1 loss for the reconstruction of organ and tumor, and Dice loss is used for optimising the mask prediction. The loss functions can be expressed as follows:

$$\mathcal{L}_0 = |\hat{x}_i - x_{n_i}| \quad (6)$$

$$\mathcal{L}_1 = |\hat{s}_i - s_i| \quad (7)$$

$$\mathcal{L}_2 = 1 - \frac{2 \cdot |\hat{m}_i \cap m_i|}{|\hat{m}_i| + |m_i|} \quad (8)$$

$$\mathcal{L}_3 = |(\alpha \cdot \hat{m}_i \cdot \hat{x}_i + (1 - \alpha \cdot \hat{m}_i) \cdot \hat{s}_i) - x_i| \quad (9)$$

$$\mathcal{L}_{\text{total}} = \lambda_0 \cdot \mathcal{L}_0 + \lambda_1 \cdot \mathcal{L}_1 + \lambda_2 \cdot \mathcal{L}_2 + \lambda_3 \cdot \mathcal{L}_3 \quad (10)$$

where $\lambda_0, \lambda_1, \lambda_2$ and λ_3 are parameters weighting the importance of each optimisation function. Note that, we directly use ground truth α to generate the reconstruction of blended input, as shown in Eq. (9), such operation has effectively forced the predicted segmentation mask m_i to be binary. For simplicity, we use $\lambda_0 = \lambda_1 = \lambda_2 = \lambda_3 = 1.0$.

Discussion. In our self-supervised training, we require the model to separately reconstruct the normal organ image and the tumor, with the assumption that the tumor should be approximately independent of its neighboring anatomies. Intuitively, this proxy task can only be solved after the model has grasped the general pattern of the normal organ, and

successfully detect the regions with irregularity. During inference, the mask prediction enables the trained model to directly generalise to the segmentation of real tumor data. Note that, after warming up with synthetic data, this training process can also include the real tumor images, *i.e.* $x_{t_i} \in \mathcal{D}_{\text{tumor}}$, and simply turn off the respective losses, by setting $\lambda_0 = \lambda_1 = \lambda_2 = 0$, $\alpha = 1$ and training degenerates to a standard reconstruction task. Experimentally, as shown in Table. V, this has been shown to further improve the performance for zero-shot tumor segmentation.

IV. EXPERIMENTS

In this section, we first introduce the datasets that we used for self-supervised learning, along with our considered downstream tasks. Then, we describe the baseline methods and the evaluation metrics, followed by the implementation details for our proposed approach.

A. Pretraining Datasets

As for self-supervised pre-training, we collect a set of raw data samples from the publicly available datasets.

Brain MRI Dataset. We collected 993 healthy brain Fluid-Attenuated Inversion Recovery (FLAIR) MRI from OASIS dataset [37], a longitudinal neuroimaging, clinical, and cognitive dataset for normal aging and Alzheimer Disease. All of the volumes are already co-registered, skull stripped and resampled into a 1-mm isotropic image in atlas space.

Abdomen CT Dataset. We collected 663 abdomen CT scans from 6 public datasets, including BTCV [38], CHAOs [39], KiTS [40], Pancreas-CT, and two subsets (*i.e.*, Pancreas and Spleen) of the Medical Segmentation Decathlon (MSD) challenge [41]. We extracted the liver ROI of all the volumes with an off-the-shelf model based on nnU-Net [20], and our self-supervised training only uses these ROIs.

B. Downstream Tasks and Benchmarks

Brain Tumor Segmentation. BraTS2018 [16] contains 285 training cases and 66 validation cases acquired by different MRI scanners. For each patient, T1 weighted, post-contrast T1-weighted, T2-weighted and FLAIR MRIs are provided. Each tumor is categorised into edema, necrosis and non-enhancing tumor and enhancing tumor. We conduct two experiments on this dataset:

- **WTS:** Whole tumor segmentation with FLAIR images. We adopt 3-fold cross validation on the training cases, in which two folds (190 patients) are for training and one fold (95 patients) for test. Each image is normalized independently by subtracting its mean and dividing by its standard deviation.
- **BTS:** Whole Tumor (WT), Enhanced Tumor (WT) and Tumor Core (TC) segmentation with four modality images. Note that, the pre-training dataset for brain tumor segmentation contains data from only one modality, FLAIR. Following the official BraTS challenge, we report the results of per class dice, sensitivity, specificity and Hausdorff

distances on the validation cases. Results are averages over three random trials. Each case is normalized individually using their mean and standard deviation.

Liver Tumor Segmentation. LiTS2017 [17] contains 131 labeled CT scans acquired at seven hospitals and research centers, with each scan being paired with the liver and liver tumor boundaries traced manually by radiologists.

- **LTS:** Liver Tumor segmentation. We select 118 CT scans with tumor and extract the liver ROI based on the liver mask. We adopt 3-fold cross validation, in which two folds (79 patients) are for training and one fold (39 patients) for test. We follow nnU-Net, using the 0.5 and 99.5 percentiles of the foreground voxels for clipping as well as the global foreground means a standard deviation for normalization on all images.

Summary: As for downstream tasks, we consider tumor segmentation in brain and liver, after self-supervised training models on two pretraining datasets respectively, and evaluate them with two different protocols. Specifically, WTS and LTS are used for evaluating the transferability and generalisability of models via supervised fine-tuning and zero-shot segmentation, while BTS is only used for supervised fine-tuning experiment, since it includes fine-grained tumor categorisation.

C. Baseline Methods

We compare against the state-of-the-art self-supervised learning approaches with official codes available. In general, these approaches can be cast into two categories, namely, single-stage (*i.e.* *unsupervised anomaly detection* [29], [30]) and two-stage (*i.e.* pre-training and fine-tuning [9], [10]) methods. In essence, all self-supervised learning approaches differ only in the definition of the proxy tasks, as described in the following:

- **3D IF** [29]: an auto-decoder is used to learn the distribution of healthy images, where implicit representation is used to map continuous spatial coordinates and latent vectors to the voxels intensities. The differences between the output restored image and input are treated as anomalies.
- **ASC-Net** [30]: an adversarial-based selective cutting neural network aims to decompose an image into two selective cuts based on a reference distribution defined by a set of normal images.
- **3D RPL** [9]: a proxy task is defined to locate the query patch relative to the central patch.
- **3D Jigsaw** [9]: a proxy task is defined to solve jigsaw puzzles on the shuffled input volumes.
- **3D Rotation** [9]: a proxy task is defined to predict the rotation degree applied on input scans.
- **Model Genesis** [10]: a proxy task is defined to recover the original data volume, from one that undergoes various artificial transformations, such as non-linear, local-shuffling, outer-cutout and inner-cutout.

D. Evaluation Metric

We quantitatively evaluate the segmentation accuracy using Dice overlap coefficient, sensitivity, specificity, and Hausdorff distance (95%), specifically:

$$\text{Dice} = \frac{2TP}{FP + 2TP + FN} \quad (11)$$

$$\text{Sensitivity} = \frac{TP}{TP + FN} \quad (12)$$

$$\text{Specificity} = \frac{TN}{TN + FP} \quad (13)$$

where TP, FP, TN, FN denote true positives, false positives, true negatives and false negatives, and Hausdorff distance is defined as:

$$d_H(X, Y) = \max \left\{ \sup_{x \in X} d(x, Y), \sup_{y \in Y} d(X, y) \right\} \quad (14)$$

$$d(x, Y) = \inf_{y \in Y} d(x, y) \quad (15)$$

with X, Y referring to predicted mask and ground truth respectively, and x, y are points on X and Y .

E. Network Architecture and Implementation Details

Network Architecture. Our proposed self-supervised learning method is flexible for any 3D encoder-decoder network. For simplicity, we adopt the commonly used 3D UNet [42] as the network backbone, which is same as in previous work [10]. It comprises an encoder and a decoder with skip connections, the encoder consists of 4 blocks, each block has two $3 \times 3 \times 3$ convolution layers followed by a batch normalization layer, a ReLU layer and a $2 \times 2 \times 2$ max-pooling layer. Symmetrically, each decoder block contains a $2 \times 2 \times 2$ deconvolution, followed by two $3 \times 3 \times 3$ convolutions with batch normalisation and ReLU. In the last layer, a $1 \times 1 \times 1$ convolution is used to reduce the number of output channels to 3, corresponding to the restored normal organ image, restored tumor and predicted mask.

Implementation Details. Our framework is trained with PyTorch on a GeForce RTX 3090 GPU with 24GB memory. At the *pre-training* stage, the volumetric input has a size of $128 \times 128 \times 128$ with mini-batch size as 2. we adopt Adam [43] with $\beta_1 = 0.9$, $\beta_2 = 0.999$, $\epsilon = 10^{-8}$. The initial learning rate was 10^{-3} and decayed with ReduceLROnPlateau scheduler. During *inference*, the predicted tumor mask can be treated as the result of zero-shot segmentation. At the *fine-tuning* stage, the pre-trained encoder is used as an initialization for the network, and a randomly initialized decoder with skip connections for supervised fine-tuning. Data augmentation during fine-tuning involves rotations, scaling, Gaussian noise, Gaussian blur, brightness, contrast, gamma and mirroring, as proposed in the nnU-Net [20]. The entire model is trained end-to-end with dice loss, using Adam [43] optimiser with an initial learning rate of 10^{-4} , and decayed with ReduceLROnPlateau scheduler.

V. RESULTS

In this section, we report the experiment results. To begin with, we fine-tune the self-supervised model end-to-end on downstream tasks, as shown in Subsection V-A. Aligning with previous work, we treat model trained from self-supervised learning as an initialization for supervised fine-tuning. Despite this is the most widely considered protocol, we argue that, this is in fact not showing the merit of self-supervised learning, as in essence, it still requires full annotation for the full downstream dataset.

Next, to better understand *the usefulness of self-supervised learning*, in Subsection V-B, we evaluate its transferability, by gradually reducing the available annotations from 100% to 0% during fine-tuning. Note that, in the extreme case with 0% annotations available, we aim to directly segment the tumor without fine-tuning, resembling the zero-shot segmentation. Our model can still work and achieve state-of-the-art performance, as discussed in Subsection V-C.

Lastly, we have conducted extensive ablation studies in Subsection V-D, to investigate the impact of different hyper-parameters during artificial “tumor” generation process and the importance of proxy tasks.

A. Fully Supervised Fine-tuning

As shown in Table I and Table II, we report the Dice, Hausdorff, Sensitivity and Specificity for all three tasks, *i.e.* WTS, LTS and BTS. In general, we can observe the following phenomena: *First*, while comparing with **Scratch (w.o. aug)**, all self-supervised approaches clearly demonstrate superior performance, however, such benefits quickly diminish once we introduce more data augmentation, *e.g.* **Scratch (w. aug)**. We consider this to be a fair comparison as aggressive data augmentations have always been built in the self-supervised pre-training process. In the following experiments, we always include the same set of augmentations during fine-tuning, unless otherwise specified. *Second*, none of the existing approaches dominate all metrics, and in fact, the variance in performance between different approaches is typically less than 2%, with the only exception from the **Sensitivity** on LTS, where **Genesis** and **Ours** substantially outperform the others. Here, the higher sensitivity indicates that these two approaches are better at detecting small tumors. In addition, our model always shows lower standard deviations in the downstream tasks, which implies the benefits of our self-supervised approach to robustness.

B. Analysis on Model Transferability

In this section, we study the usefulness of self-supervised learning by varying the number of available volume annotations. Specifically, the self-supervised models are fine-tuned on different ratios of annotations, and evaluate on the same test set. As shown in Table III, we conduct experiments on WTS and LTS, for both tasks, our proposed method shows superior performance on all supervision levels, impressively, our self-supervised model really shines under a low-data regime, *e.g.* 10% or zero-shot segmentation, an extreme case

TABLE I

COMPARE WITH SOTA SELF-SUPERVISED METHODS ON WTS (BRAIN WHOLE TUMOR SEGMENTATION) AND LTS (LIVER TUMOR SEGMENTATION). WE REPORT THE RESULTS OF MEAN \pm STD OVER 3-FOLD CROSS VALIDATION.

Method	Dice (%) \uparrow		Hausdorff (mm) \downarrow		Sensitivity (%) \uparrow		Specificity (%) \uparrow	
	WTS	LTS	WTS	LTS	WTS	LTS	WTS	LTS
Scratch (w.o. aug)	83.32 \pm 2.42	58.30 \pm 2.93	9.84 \pm 1.16	40.15 \pm 3.61	80.49 \pm 2.56	59.15 \pm 7.56	99.89 \pm 0.02	99.64 \pm 1.45
Scratch (w. aug)	86.03 \pm 0.90	60.04 \pm 4.03	7.45 \pm 0.24	30.70 \pm 5.87	85.21 \pm 2.93	59.19 \pm 7.83	99.90 \pm 0.03	99.79 \pm 1.04
3D RPL	85.64 \pm 0.34	60.15 \pm 4.36	8.60 \pm 1.37	32.39 \pm 5.84	86.06 \pm 2.21	59.21 \pm 9.23	99.88 \pm 0.01	99.73 \pm 1.91
3D Jigsaw	84.95 \pm 0.97	59.13 \pm 5.12	9.01 \pm 0.54	29.20 \pm 3.66	83.20 \pm 7.84	59.54 \pm 9.90	99.90 \pm 0.02	99.68 \pm 2.72
3D Rotation	84.35 \pm 1.12	59.72 \pm 4.87	10.98 \pm 2.65	33.33 \pm 16.56	84.21 \pm 2.25	59.91 \pm 8.57	99.89 \pm 0.01	99.86 \pm 0.05
Genesis	85.62 \pm 0.48	61.34 \pm 4.26	8.01 \pm 0.77	39.92 \pm 8.90	84.56 \pm 1.30	65.59 \pm 10.11	99.90 \pm 0.02	99.73 \pm 1.74
Ours	86.13 \pm 0.91	61.91 \pm 2.71	8.11 \pm 0.54	31.41 \pm 8.33	85.49 \pm 2.96	65.39 \pm 3.72	99.90 \pm 0.01	99.73 \pm 1.89

TABLE II

COMPARE WITH SOTA SELF-SUPERVISED METHODS ON BTS (WHOLE TUMOR, TUMOR CORE AND ENHANCED TUMOR SEGMENTATION). WE REPORT THE RESULTS OF MEAN \pm STD BY FIXED THE TRAINING SET AND RUN THREE DIFFERENT SEEDS.

Method	Dice (%) \uparrow			Hausdorff (mm) \downarrow			Sensitivity (%) \uparrow			Specificity (%) \uparrow		
	WT	TC	ET	WT	TC	ET	WT	TC	ET	WT	TC	ET
Scratch (w.o. aug)	84.23 \pm 0.95	64.44 \pm 3.65	69.31 \pm 5.08	19.94 \pm 3.97	19.85 \pm 1.03	10.98 \pm 1.83	83.07 \pm 0.97	71.89 \pm 3.44	67.80 \pm 1.30	99.35 \pm 1.60	99.21 \pm 0.94	99.85 \pm 0.01
Scratch (w. aug)	89.70 \pm 0.27	80.53 \pm 0.25	77.15 \pm 0.31	9.47 \pm 5.10	8.50 \pm 1.88	3.76 \pm 1.38	90.35 \pm 0.10	77.48 \pm 0.52	79.60 \pm 0.34	99.47 \pm 0.04	99.87 \pm 0.06	99.83 \pm 0.01
3D RPL	88.40 \pm 1.64	80.92 \pm 1.06	77.04 \pm 0.44	10.59 \pm 6.03	8.96 \pm 0.69	6.15 \pm 2.01	87.71 \pm 2.98	79.33 \pm 0.99	80.57 \pm 1.68	99.56 \pm 0.06	99.84 \pm 0.01	99.81 \pm 0.02
3D Jigsaw	89.33 \pm 0.32	79.07 \pm 0.35	76.12 \pm 0.19	8.42 \pm 4.26	9.67 \pm 1.98	5.01 \pm 0.42	89.84 \pm 0.46	78.58 \pm 1.78	79.76 \pm 0.60	99.46 \pm 0.06	99.80 \pm 0.06	99.82 \pm 0.01
3D Rotation	89.22 \pm 0.35	78.82 \pm 0.27	74.92 \pm 1.42	10.45 \pm 1.33	10.67 \pm 2.17	5.88 \pm 1.73	89.72 \pm 0.71	78.32 \pm 2.21	78.94 \pm 1.38	99.42 \pm 0.08	99.81 \pm 0.07	99.82 \pm 0.01
Genesis	90.10 \pm 0.64	82.77 \pm 0.26	75.78 \pm 0.36	6.36 \pm 1.21	7.63 \pm 1.04	4.68 \pm 1.24	89.96 \pm 1.51	82.52 \pm 2.04	82.23 \pm 2.16	99.54 \pm 0.06	99.80 \pm 0.05	99.80 \pm 0.02
Ours	90.10 \pm 0.51	82.47 \pm 0.84	77.32 \pm 0.06	5.89 \pm 0.40	7.78 \pm 0.75	4.38 \pm 0.60	90.05 \pm 0.30	80.01 \pm 0.55	81.39 \pm 0.64	99.54 \pm 0.01	99.80 \pm 0.01	99.86 \pm 0.01

TABLE III

COMPARE WITH SOTA SELF-SUPERVISED METHODS BY FINE-TUNING ON DIFFERENT RATIO OF LABELED DATA.

Method	WTS (Dice% \uparrow)						LTS (Dice% \uparrow)					
	0	0.1	0.2	0.4	0.6	0.8	0	0.1	0.2	0.4	0.6	0.8
Scratch (w. aug)	8.62	77.18	77.10	81.47	83.46	83.75	3.52	45.43	52.96	52.80	53.57	56.59
Genesis	6.13	77.29	77.49	80.35	83.62	83.96	2.01	48.87	54.37	54.21	57.93	58.72
3D RPL	6.79	78.85	79.00	81.68	82.63	84.29	3.11	49.25	49.51	55.53	56.93	57.60
Ours	71.63	79.80	79.66	82.64	83.92	84.49	40.78	53.61	54.84	57.74	59.36	60.52

with 0% annotation available, clearly outperforming all other approaches that can only give random predictions.

C. Analysis on Model Generalisability

In this section, we compare with state-of-the-art approaches that are designed for unsupervised anomaly detection. Due to the unavailability of official codes, we compare with previous methods by evaluating on the same setting, *e.g.* dataset. As shown in Table IV, our approach surpasses the other ones by a large margin, in particular, on brain tumor segmentation (WTS), we substantially improve the Dice score over the recent state-of-the-art methods from 67.20% to 71.66%, and from 32.24% to 40.78% on liver tumor segmentation (LTS).

In Fig 4, we show qualitative results from our self-supervised model on real tumor data under a zero-shot setting,

i.e. models are directly adopted for mask prediction *without* using any manual annotation whatsoever. As can be seen, our method accurately detects and segments the tumors, along with the intensity distribution of the restored image closely resembling that of the normal organ, effectively inpainting the tumor regions. This indicates that our model can generalise well to a previously unseen dataset without any retraining. For more qualitative results, we refer the readers to our project page.

D. Ablation studies

In this section, we conduct ablation studies to understand the effect of different choices on artificial transformations in simulation and the proxy tasks. In both sections, we train

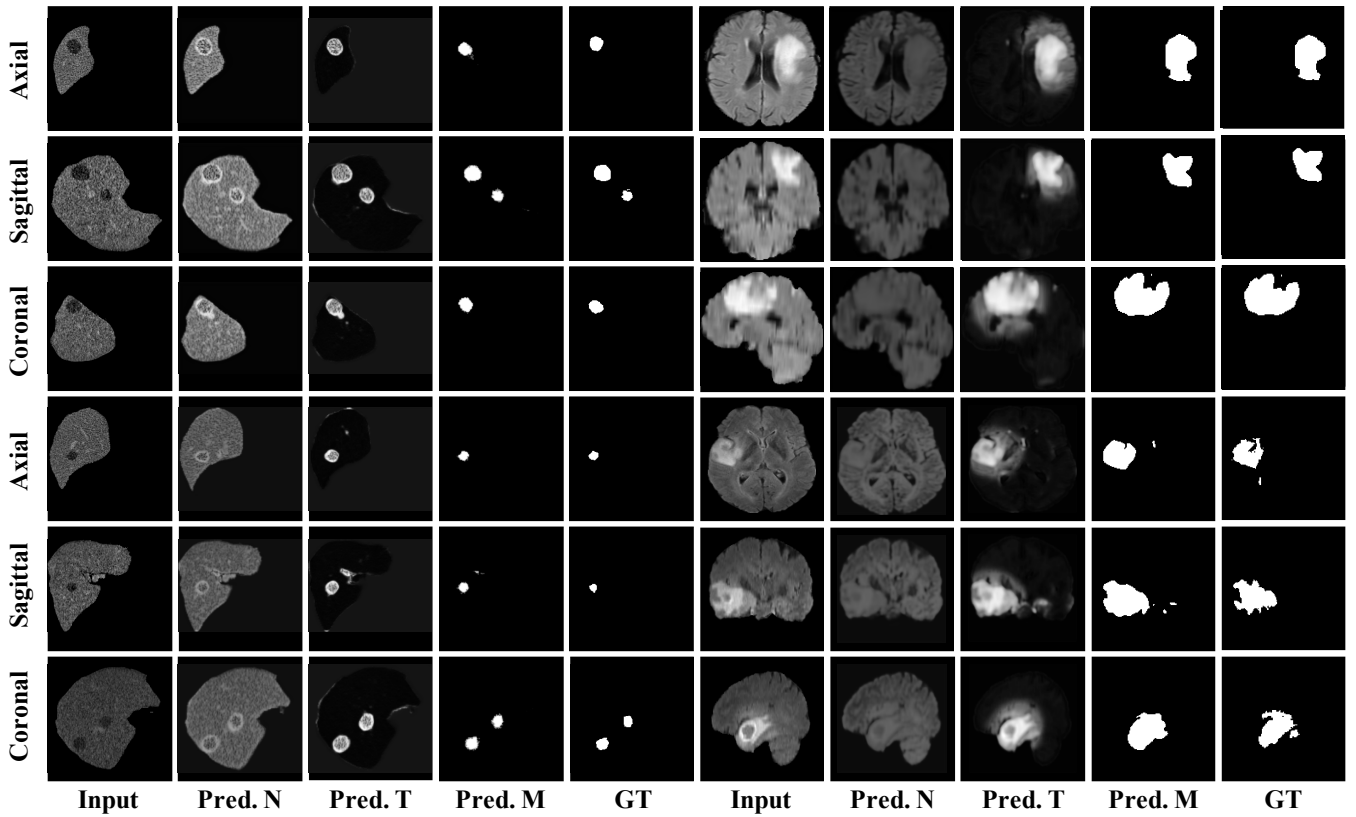


Fig. 4. Zero-shot tumor segmentation from our self-supervised model on real tumor data sampled on axial, coronal, and sagittal views. The first five columns show the results of liver tumor, which corresponds to [Input, Predicted normal image (Pred.N), Predicted tumor image (Pred.T), Predicted mask (Pred.M), Ground Truth (GT)]. The last five columns show the results of brain tumors.

TABLE IV

COMPARE WITH SOTA UNSUPERVISED ANOMALY SEGMENTATION METHODS ON WHOLE TUMOR SEGMENTATION.

Method	Year	Supervision	Dice (%) \uparrow	
			WTS	LTS
Scratch (w. aug)	–	✓	86.03 \pm 0.90	60.04 \pm 4.03
3D IF	2021	✗	67.20 \pm 15.5*	–
ASC-Net	2021	✗	63.67*	32.24*
Ours	2021	✗	71.63 \pm 0.84	40.78 \pm 0.43

Results with * are directly copied from original papers [29], [30].

multiple self-supervised models by varying one factor at a time, and report zero-shot segmentation results.

On Data Simulation. To begin with, we estimate a performance upper bound for our proposed simulation process, specifically, assuming the tumor segmentation masks are indeed available, we can thus blend normal image with tumors cropped from ground truth masks.

As summarised in Table V, we make the following observations: (1) Comparing to the case where no transformation is adopted, *i.e.* directly blend one region cropped from another image, artificial transformations always bring significant improvement, demonstrating the necessity of designing suitable transformations. (2) Linear transformation acts as the basis for all the transformations. This is consistent with the fact that intensity contrast has always been an effective cue to

TABLE V

ABLATION STUDY ON DATA SIMULATION. RESULTS ARE REPORTED FOR ZERO SHOT TUMOR SEGMENTATION.

Transformation			Target task	
Intensity	Blur	Elastic	WTS (Dice% \uparrow)	LTS (Dice% \uparrow)
✓			52.62	5.88
			67.64	33.95
			62.28	10.1
		✓	59.91	3.47
✓	✓		69.53	38.91
✓		✓	70.97	36.15
✓	✓	✓	71.63	40.78
Real tumor (Upper Bound)			72.83	42.58

differentiate lesions from normal organs. (3) Our simulated tumor shows comparable results with the estimated upper bound.

On Proxy Tasks. Here, we conduct studies to verify the usefulness of different losses in Eq 11. As shown in Table VI, we first summarise the different combinations of proxy task as follows: (1) \mathcal{L}_0 , refers to a restoration task that recovers the normal organ from tumor input, and segmentation can be obtained by thresholding the reconstruction error; (2) \mathcal{L}_2 , refers to the proxy task for segmenting synthetic anomalies with discriminative training; (3) $\mathcal{L}_0 + \mathcal{L}_1$, learns to distinguish the abnormal region by reconstructing both the normal and tumor parts; (4) $\mathcal{L}_0 + \mathcal{L}_1 + \mathcal{L}_2$, refers to training without

TABLE VI

ABLATION STUDY ON LOSS FUNCTION. RESULTS ARE REPORTED FOR ZERO SHOT TUMOR SEGMENTATION.

Optimise function	WTS (Dice%)	LTS (Dice%)
\mathcal{L}_0	38.47	7.24
\mathcal{L}_2	66.84	37.09
$\mathcal{L}_0 + \mathcal{L}_1$	64.66	33.08
$\mathcal{L}_0 + \mathcal{L}_1 + \mathcal{L}_2$	70.92	40.07
$\mathcal{L}_0 + \mathcal{L}_1 + \mathcal{L}_2 + \mathcal{L}_3$	71.66	40.78
Ours (w real tumor data)	72.62	41.08

restoring input volume; (5) $\mathcal{L}_0 + \mathcal{L}_1 + \mathcal{L}_2 + \mathcal{L}_3$, refers to the full self-supervised learning approach we proposed; (6) *Ours* (w real tumor data), denotes the case, where real tumor data is also introduced to the training process, though only the full volume reconstruction (\mathcal{L}_3) is adopted.

From the experimental results, we can observe that the segmentation from restoration (\mathcal{L}_0) is far from being satisfactory, this is not surprising as such proxy task is not specifically designed for the tumor segmentation task. In contrast, learning to segment synthetic anomalies with a discriminative loss (\mathcal{L}_2) substantially improves the segmentation results, and combining all proxy tasks give the best performance. Besides, when introducing real tumor data to the training process, despite only the volume reconstruction (\mathcal{L}_3) is available, the involvement of real tumor samples is still beneficial to bridge the domain gap between simulated and real data, thus, enhance the zero-shot generalisation.

VI. CONCLUSION

To conclude, in this paper, we propose a novel self-supervised learning method for 3D tumor segmentation, exploiting synthetic data to train a “layer decomposition” model. The key difference to the conventional self-supervised learning model is that, our model can be directly applied to the downstream tumor segmentation task, advocating the zero-shot tumor segmentation. To validate the effectiveness of our approach, we conducted extensive experiments on two benchmarks: BraTS2018 for brain tumor segmentation and LiTS2017 for liver tumor segmentation, and show superior performance on transferability and generalisability to strong baselines and other state-of-the-art methods.

REFERENCES

- [1] H. Seo, C. Huang, M. Bassenne, R. Xiao, and L. Xing, “Modified u-net (mu-net) with incorporation of object-dependent high level features for improved liver and liver-tumor segmentation in ct images,” *IEEE Transactions on Medical Imaging*, vol. 39, no. 5, pp. 1316–1325, 2020.
- [2] J. Jiang, Y.-C. Hu, C.-J. Liu, D. Halpenny, M. D. Hellmann, J. O. Deasy, G. Mageras, and H. Veeraraghavan, “Multiple resolution residually connected feature streams for automatic lung tumor segmentation from ct images,” *IEEE Transactions on Medical Imaging*, vol. 38, no. 1, pp. 134–144, 2019.
- [3] Q. Yu, Y. Shi, J. Sun, Y. Gao, J. Zhu, and Y. Dai, “Crossbar-net: A novel convolutional neural network for kidney tumor segmentation in ct images,” *IEEE Transactions on Image Processing*, vol. 28, no. 8, pp. 4060–4074, 2019.
- [4] S. Pereira, A. Pinto, V. Alves, and C. A. Silva, “Brain tumor segmentation using convolutional neural networks in mri images,” *IEEE Transactions on Medical Imaging*, vol. 35, no. 5, pp. 1240–1251, 2016.
- [5] A. Işın, C. Direkçioğlu, and M. Şah, “Review of mri-based brain tumor image segmentation using deep learning methods,” *Procedia Computer Science*, vol. 102, pp. 317–324, 2016.
- [6] L. Jing and Y. Tian, “Self-supervised visual feature learning with deep neural networks: A survey,” *IEEE Transactions on Pattern Analysis and Machine Intelligence*, no. 01, pp. 1–1, 2020.
- [7] X. Zhuang, Y. Li, Y. Hu, K. Ma, Y. Yang, and Y. Zheng, “Self-supervised feature learning for 3d medical images by playing a rubik’s cube,” in *Medical Image Computing and Computer Assisted Intervention*, pp. 420–428, 2019.
- [8] L. Chen, P. Bentley, K. Mori, K. Misawa, M. Fujiwara, and D. Rueckert, “Self-supervised learning for medical image analysis using image context restoration,” *Medical Image Analysis*, vol. 58, p. 101539, 2019.
- [9] A. Taleb, W. Loetzsch, N. Danz, J. Severin, T. Gaertner, B. Bergner, and C. Lippert, “3d self-supervised methods for medical imaging,” in *Advances in Neural Information Processing Systems*, vol. 33, pp. 18158–18172, 2020.
- [10] Z. Zhou, V. Sodha, M. M. R. Siddiquee, R. Feng, N. Tajbakhsh, M. B. Gotway, and J. Liang, “Models genesis: Generic autodidactic models for 3d medical image analysis,” in *Medical Image Computing and Computer Assisted Intervention*, pp. 384–393, 2019.
- [11] P. H. Yeung, A. Namburete, and W. Xie, “Sli2vol: Annotate a 3d volume from a single slice with self-supervised learning,” in *Medical Image Computing and Computer Assisted Intervention*, 2021.
- [12] K. Chaitanya, E. Erdil, N. Karani, and E. Konukoglu, “Contrastive learning of global and local features for medical image segmentation with limited annotations,” *Advances in Neural Information Processing Systems*, vol. 33, 2020.
- [13] F. Haghighi, M. Taher, Z. Zhou, M. Gotway, and J. Liang, “Transferable visual words: Exploiting the semantics of anatomical patterns for self-supervised learning,” *IEEE Transactions on Medical Imaging*, pp. 1–1, 2021.
- [14] Y. Xie, J. Zhang, Z. Liao, Y. Xia, and C. Shen, “Pgl: Prior-guided local self-supervised learning for 3d medical image segmentation,” 2020.
- [15] J. Wang and E. Adelson, “Layered representation for motion analysis,” in *Proceedings of IEEE Conference on Computer Vision and Pattern Recognition*, pp. 361–366, 1993.
- [16] B. H. Menze et al., “The multimodal brain tumor image segmentation benchmark (brats),” *IEEE Transactions on Medical Imaging*, vol. 34, no. 10, pp. 1993–2024, 2015.
- [17] P. Bilic, P. F. Christ, E. Vorontsov, G. Chlebus, H. Chen, Q. Dou, C.-W. Fu, X. Han, P.-A. Heng, J. Hesser, and et al., “The liver tumor segmentation benchmark (lits),” 2019.
- [18] X. Li, H. Chen, X. Qi, Q. Dou, C.-W. Fu, and P.-A. Heng, “H-denseunet: Hybrid densely connected unet for liver and tumor segmentation from ct volumes,” *IEEE Transactions on Medical Imaging*, vol. 37, no. 12, pp. 2663–2674, 2018.
- [19] P. Ahmad, S. Qamar, L. Shen, and A. Saeed, “Context aware 3d unet for brain tumor segmentation,” in *Brainlesion: Glioma, Multiple Sclerosis, Stroke and Traumatic Brain Injuries*, pp. 207–218, 2021.
- [20] F. Isensee, P. F. Jaeger, S. A. A. Kohl, J. Petersen, and K. H. Maier-Hein, “nnu-net: a self-configuring method for deep learning-based biomedical image segmentation,” *Nature Methods*, vol. 18, pp. 203–211, 2021.
- [21] V. Cheplygina, M. de Bruijne, and J. P. Pluim, “Not-so-supervised: A survey of semi-supervised, multi-instance, and transfer learning in medical image analysis,” *Medical Image Analysis*, vol. 54, pp. 280–296, 2019.
- [22] S. Min, X. Chen, Z.-J. Zha, and Y. Zhang, “A two-stream mutual attention network for semi-supervised biomedical segmentation with noisy labels,” *Proceedings of the AAAI Conference on Artificial Intelligence*, vol. 33, pp. 4578–4585, 2019.
- [23] S. Chen, G. Bortsova, A. García-Uceda Juárez, G. van Tulder, and M. de Bruijne, “Multi-task attention-based semi-supervised learning for medical image segmentation,” in *Medical Image Computing and Computer Assisted Intervention*, pp. 457–465, 2019.
- [24] W. Bai, C. Chen, G. Tarroni, J. Duan, F. Guitton, S. Petersen, Y. Guo, P. Matthews, and D. Rueckert, “Self-supervised learning for cardiac mr image segmentation by anatomical position prediction,” in *Medical Image Computing and Computer Assisted Intervention*, pp. 541–549, 2019.
- [25] J. Gildenblat and E. Klaiman, “Self-supervised similarity learning for digital pathology,” in *Medical Image Computing and Computer Assisted Intervention Workshop*, 2019.
- [26] F. Liu, Y. Jonmohamadi, G. Maicas, A. Pandey, and G. Carneiro, “Self-supervised depth estimation to regularise semantic segmentation in knee arthroscopy,” in *Medical Image Computing and Computer Assisted Intervention*, 2019.

- [27] X. Zhang, S. Feng, Y. Zhou, Y. Zhang, and Y. Wang, "Sar: Scale-aware restoration learning for 3d tumor segmentation," in *Medical Image Computing and Computer Assisted Intervention*, 2021.
- [28] C. Baur, S. Denner, B. Wiestler, N. Navab, and S. Albarqouni, "Autoencoders for unsupervised anomaly segmentation in brain mr images: A comparative study," *Medical Image Analysis*, vol. 69, p. 101952, 2021.
- [29] S. N. Marimont and G. Tarroni, "Implicit field learning for unsupervised anomaly detection in medical images," in *Medical Image Computing and Computer Assisted Intervention*, 2021.
- [30] R. Dey and Y. Hong, "Asc-net : Adversarial-based selective network for unsupervised anomaly segmentation," in *Medical Image Computing and Computer Assisted Intervention*, 2021.
- [31] G. Pang, C. Shen, L. Cao, and A. V. Hengel, "Deep learning for anomaly detection," *ACM Computing Surveys (CSUR)*, vol. 54, pp. 1–38, 2021.
- [32] Y. Fei, C. Huang, C. Jinkun, M. Li, Y. Zhang, and C. Lu, "Attribute restoration framework for anomaly detection," *IEEE Transactions on Multimedia*, pp. 1–1, 2020.
- [33] B. Zong, Q. Song, M. R. Min, W. Cheng, C. Lumezanu, D. ki Cho, and H. Chen, "Deep autoencoding gaussian mixture model for unsupervised anomaly detection," in *ICLR*, 2018.
- [34] M.-S. To, I. G. Sarno, C. Chong, M. Jenkinson, and G. Carneiro, "Self-supervised lesion change detection and localisation in longitudinal multiple sclerosis brain imaging," in *Medical Image Computing and Computer Assisted Intervention*, 2021.
- [35] J. Tan, B. Hou, T. G. Day, J. Simpson, D. Rueckert, and B. Kainz, "Detecting outliers with poisson image interpolation," in *Medical Image Computing and Computer Assisted Intervention*, 2021.
- [36] F. Pérez-García, R. Dorent, M. Rizzi, F. Cardinale, V. Frazzini, V. Navarro, C. Essert, I. Ollivier, T. Vercauteren, R. Sparks, *et al.*, "A self-supervised learning strategy for postoperative brain cavity segmentation simulating resections," *International Journal of Computer Assisted Radiology and Surgery*, pp. 1–9, 2021.
- [37] M. DS, F. AF, C. JG, M. JC, and B. RL., "Open access series of imaging studies: longitudinal mri data in nondemented and demented older adults," *Journal of Cognitive Neuroscience*, vol. 22, pp. 2677–84, 2018.
- [38] B. Landman, Z. Xu, J. E. Igelsias, M. Styner, T. R. Langerak, and A. Klein., "Multi-atlas labeling beyond the cranial vault – workshop and challenge," *Journal of Clinical Oncology*, 2015.
- [39] A. E. Kavur, N. S. Gezer, M. Barış, S. Aslan, P.-H. Conze, V. Groza, D. D. Pham, S. Chatterjee, P. Ernst, S. Özkan, and *et al.*, "Chaos challenge - combined (ct-mr) healthy abdominal organ segmentation," *Medical Image Analysis*, vol. 69, p. 101950, 2021.
- [40] N. Heller, S. McSweeney, M. T. Peterson, S. Peterson, J. Rickman, B. Stai, R. Tejapaul, M. Oestreich, and *et al.*, "An international challenge to use artificial intelligence to define the state-of-the-art in kidney and kidney tumor segmentation in ct imaging," *Journal of Clinical Oncology*, vol. 38, pp. 626–626, 2020.
- [41] A. L. Simpson, M. Antonelli, S. Bakas, M. Bilello, K. Farahani, B. van Ginneken, A. Kopp-Schneider, B. A. Landman, G. Litjens, B. Menze, and *et al.*, "A large annotated medical image dataset for the development and evaluation of segmentation algorithms," 2019.
- [42] Ö. Çiçek, A. Abdulkadir, S. S. Lienkamp, T. Brox, and O. Ronneberger, "3d u-net: Learning dense volumetric segmentation from sparse annotation," in *Medical Image Computing and Computer Assisted Intervention*, pp. 424–432, 2016.
- [43] D. Kingma and J. Ba, "Adam: A method for stochastic optimization," in *International Conference on Learning Representations*, vol. 42, 2014.